

## Compact gas cell integrated with a linear variable optical filter

Ayerden, N.P.; Graaf, G. de; Wolffenbuttel, R.F.

**DOI**

[10.1364/OE.24.002981](https://doi.org/10.1364/OE.24.002981)

**Publication date**

2016

**Document Version**

Final published version

**Published in**

Optics Express

**Citation (APA)**

Ayerden, N. P., Graaf, G. D., & Wolffenbuttel, R. F. (2016). Compact gas cell integrated with a linear variable optical filter. *Optics Express*, 24(3), 2981-3002. <https://doi.org/10.1364/OE.24.002981>

**Important note**

To cite this publication, please use the final published version (if applicable). Please check the document version above.

**Copyright**

Other than for strictly personal use, it is not permitted to download, forward or distribute the text or part of it, without the consent of the author(s) and/or copyright holder(s), unless the work is under an open content license such as Creative Commons.

**Takedown policy**

Please contact us and provide details if you believe this document breaches copyrights. We will remove access to the work immediately and investigate your claim.

# Compact gas cell integrated with a linear variable optical filter

N. Pelin Ayerden,\* Ger de Graaf, and Reinoud F. Wolffenbuttel

Electronic Instrumentation Laboratory, Microelectronics Department, Faculty of EEMCS, Delft University of Technology, Mekelweg 4, 2628 CD, Delft, The Netherlands

\*n.p.ayerden@tudelft.nl

**Abstract:** A miniaturized methane (CH<sub>4</sub>) sensor based on nondispersive infrared absorption is realized in MEMS technology. A high level of functional integration is achieved by using the resonance cavity of a linear variable optical filter (LVOF) also as a gas absorption cell. For effective detection of methane at  $\lambda = 3.39 \mu\text{m}$ , an absorption path length of at least 5 mm is required. Miniaturization therefore necessitates the use of highly reflective mirrors and operation at the 15th-order mode with a resonator cavity length of 25.4  $\mu\text{m}$ . The conventional description of the LVOF in terms of the Fabry-Perot resonator is inadequate for analyzing the optical performance at such demanding boundary conditions. We demonstrate that an approach employing the Fizeau resonator is more appropriate. Furthermore, the design and fabrication in a CMOS-compatible microfabrication technology are described and operation as a methane sensor is demonstrated.

©2016 Optical Society of America

**OCIS codes:** (280.4788) Optical sensing and sensors; (300.6340) Spectroscopy, infrared; (310.6845) Thin film devices and applications; (120.2230) Fabry-Perot; (230.1480) Bragg reflectors; (230.3990) Micro-optical devices.

---

## References and links

1. R. F. Wolffenbuttel, "MEMS-based optical mini- and microspectrometers for the visible and infrared spectral range," *J. Micromech. Microeng.* **15**(7), S145–S152 (2005).
2. R. A. Crocombe, "Miniature Optical Spectrometers: There's Plenty of Room at the Bottom. Part I: Background and Mid-Infrared Spectrometers," *Spectroscopy* (Springf.) **23**(1), 38–56 (2008).
3. J. H. Jerman, D. J. Clift, and S. R. Mallinson, "A miniature Fabry-Perot interferometer with a corrugated silicon diaphragm support," *Sensor. Actuat. A-Phys.* **29**(2), 151–158 (1991).
4. S. Grabarnik, A. Emadi, H. Wu, G. de Graaf, and R. F. Wolffenbuttel, "High-resolution microspectrometer with an aberration-correcting planar grating," *Appl. Opt.* **47**(34), 6442–6447 (2008).
5. S. Grabarnik, R. Wolffenbuttel, A. Emadi, M. Loktev, E. Sokolova, and G. Vdovin, "Planar double-grating microspectrometer," *Opt. Express* **15**(6), 3581–3588 (2007).
6. N. Pelin Ayerden, U. Aygun, S. T. S. Holmstrom, S. Olcer, B. Can, J.-L. Stehle, and H. Urey, "High-speed broadband FTIR system using MEMS," *Appl. Opt.* **53**(31), 7267–7272 (2014).
7. J. H. Correia, M. Bartek, and R. F. Wolffenbuttel, "Bulk-micromachined tunable Fabry-Perot microinterferometer for the visible spectral range," *Sensor. Actuat. A-Phys.* **76**(1–3), 191–196 (1999).
8. J. Mohr, B. Anderer, and W. Ehrfeld, "Fabrication of a planar grating spectrograph by deep-etch lithography with synchrotron radiation," *Sensor. Actuat. A-Phys.* **27**(1), 571–575 (1991).
9. J. Hodgkinson and R. P. Tatam, "Optical gas sensing: a review," *Meas. Sci. Technol.* **24**(1), 012004 (2013).
10. S. Thiele and R. Salzer, "Optical Spectroscopy," in *Handbook of Spectroscopy* (Wiley, 2003), pp. 441–468.
11. S. Gersen, M. van Essen, G. van Dijk, and H. Levinsky, "Physicochemical effects of varying fuel composition on knock characteristics of natural gas mixtures," *Combust. Flame* **161**(10), 2729–2737 (2014).
12. R. Wolffenbuttel, *Silicon sensors and Circuits: On-chip Compatibility* (Springer Science & Business Media, 1996).
13. S. E. Stein, "Infrared Spectra," in *NIST Chemistry WebBook, NIST Standard Reference Database Number 69*, Eds. P. J. Linstrom and W. G. Mallard (National Institute of Standards and Technology, 2015).
14. V. Nagali, S. I. Chou, D. S. Baer, R. K. Hanson, and J. Segall, "Tunable diode-laser absorption measurements of methane at elevated temperatures," *Appl. Opt.* **35**(21), 4026–4032 (1996).
15. C. R. Webster, G. J. Flesch, D. C. Scott, J. E. Swanson, R. D. May, W. S. Woodward, C. Gmachl, F. Capasso, D. L. Sivco, J. N. Baillargeon, A. L. Hutchinson, and A. Y. Cho, "Quantum-cascade laser measurements of stratospheric methane and nitrous oxide," *Appl. Opt.* **40**(3), 321–326 (2001).

16. C. Massie, G. Stewart, G. McGregor, and J. R. Gilchrist, "Design of a portable optical sensor for methane gas detection," *Sensor. Actuat. Biol. Chem.* **113**(2), 830–836 (2006).
17. N. Neumann, M. Ebermann, S. Kurth, and K. Hiller, "Tunable infrared detector with integrated micromachined Fabry-Perot filter," *J. Micro-Nanolith. MEM* **7**(2), 021004 (2008).
18. S. Haisheng, L. Changzheng, C. Xuyuan, C. Ranbin, and Z. Qiang, "Silicon-Based Micro-Machined Infrared Emitters With a Micro-Bridge and a Self-Heating Membrane Structure," *IEEE Photonic. Tech. L.* **25**(11), 1014–1016 (2013).
19. J. Hildenbrand, J. Korvink, J. Wollenstein, C. Peter, A. Kurzinger, F. Naumann, M. Ebert, and F. Lamprecht, "Micromachined mid-infrared emitter for fast transient temperature operation for optical gas sensing systems," *IEEE Sens. J.* **10**(2), 353–362 (2010).
20. W. Konz, J. Hildenbrand, M. Bauersfeld, S. Hartwig, A. Lambrecht, V. Lehmann, and J. Wollenstein, "Micromachined IR-source with excellent blackbody like behaviour (Invited Paper)," *Proc. SPIE* **5836**, 540–548 (2005).
21. J. Antila, A. Miranto, J. Mäkynen, M. Laamanen, A. Rissanen, M. Blomberg, H. Saari, and J. Malinen, "MEMS and piezo actuator-based Fabry-Perot interferometer technologies and applications at VTT," *Proc. SPIE* **7680**, 76800U (2010).
22. J. H. Correia, G. de Graaf, S. H. Kong, M. Bartek, and R. F. Wolffenbuttel, "Single-chip CMOS optical microspectrometer," *Sensor. Actuat. A-Phys.* **82**(1–3), 191–197 (2000).
23. A. Emadi, H. Wu, G. de Graaf, and R. Wolffenbuttel, "Design and implementation of a sub-nm resolution microspectrometer based on a Linear-Variable Optical Filter," *Opt. Express* **20**(1), 489–507 (2012).
24. M. Ghaderi, N. P. Ayerden, A. Emadi, P. Enoksson, J. H. Correia, G. de Graaf, and R. F. Wolffenbuttel, "Design, fabrication and characterization of infrared LVOFs for measuring gas composition," *J. Micromech. Microeng.* **24**(8), 084001 (2014).
25. K. Hirabayashi, H. Tsuda, and T. Kurokawa, "Tunable liquid-crystal Fabry-Perot interferometer filter for wavelength-division multiplexing communication systems," *J. Lightwave Technol.* **11**(12), 2033–2043 (1993).
26. J. S. Milne, J. M. Dell, A. J. Keating, and L. Faraone, "Widely Tunable MEMS-Based Fabry-Perot Filter," *J. Microelectromech. Syst.* **18**(4), 905–913 (2009).
27. J. S. Patel, "Electrically tunable ferroelectric liquid-crystal Fabry-Perot filter," *Opt. Lett.* **17**(6), 456–458 (1992).
28. R. Rubio, J. Santander, J. Fonollosa, L. Fonseca, I. Gràcia, C. Cané, M. Moreno, and S. Marco, "Exploration of the metrological performance of a gas detector based on an array of unspecific infrared filters," *Sensor. Actuat. Biol. Chem.* **116**(1–2), 183–191 (2006).
29. W. Hu, Z. Ye, L. Liao, H. Chen, L. Chen, R. Ding, L. He, X. Chen, and W. Lu, " $128 \times 128$  long-wavelength/mid-wavelength two-color HgCdTe infrared focal plane array detector with ultralow spectral cross talk," *Opt. Lett.* **39**(17), 5184–5187 (2014).
30. F. Niklaus, C. Vieider, and H. Jakobsen, "MEMS-based uncooled infrared bolometer arrays: a review," *Proc. SPIE* **6836**, 68360D (2007).
31. D. F. Swinehart, "The Beer-Lambert Law," *J. Chem. Educ.* **39**(7), 333 (1962).
32. D. A. Jackson, "The Spherical Fabry-Perot Interferometer as an Instrument of High Resolving Power for Use with External or with Internal Atomic Beams," *Proc. R. Soc. Lon. Ser-A* **263**(1314), 289–308 (1961).
33. A. Kastler, "Atomes à l'Intérieur d'un Interféromètre Perot-Fabry," *Appl. Opt.* **1**(1), 17–24 (1962).
34. G. Hernandez, "Fabry-Perot with an absorbing etalon cavity," *Appl. Opt.* **24**(18), 3062–3067 (1985).
35. A. E. Siegman, *Lasers* (University Science Books, 1986).
36. E. D. Palik, H. Boukari, and R. W. Gammon, "Experimental study of the effect of surface defects on the finesse and contrast of a Fabry-Perot interferometer," *Appl. Opt.* **35**(1), 38–50 (1996).
37. M. Born and E. Wolf, *Principles of Optics: Electromagnetic Theory of Propagation, Interference and Diffraction of Light*, 7 ed. (Cambridge University, 1999).
38. A. D. Rakić, A. B. Djurišić, J. M. Elazar, and M. L. Majewski, "Optical properties of metallic films for vertical-cavity optoelectronic devices," *Appl. Opt.* **37**(22), 5271–5283 (1998).
39. R. Bünnagel, H. A. Oehring, and K. Steiner, "Fizeau Interferometer for Measuring the Flatness of Optical Surfaces," *Appl. Opt.* **7**(2), 331–335 (1968).
40. J. Brosset, "Multiple-beam localized fringes: Part I-Intensity distribution and localization," *Proc. Phys. Soc.* **59**(2), 224–234 (1947).
41. M. A. Rob, "Limitation of a wedged etalon for high-resolution linewidth measurements," *Opt. Lett.* **15**(11), 604–606 (1990).
42. T. T. Kajava, H. M. Lauranto, and R. R. E. Salomaa, "Fizeau interferometer in spectral measurements," *J. Opt. Soc. Am. B* **10**(11), 1980–1989 (1993).
43. P. Langenbeck, "Fizeau interferometer-fringe sharpening," *Appl. Opt.* **9**(9), 2053–2058 (1970).
44. Y. H. Meyer, "Fringe shape with an interferential wedge," *J. Opt. Soc. Am.* **71**(10), 1255–1263 (1981).
45. J. R. Rogers, "Fringe shifts in multiple-beam Fizeau interferometry," *J. Opt. Soc. Am.* **72**(5), 638–643 (1982).
46. R. R. McLeod and T. Honda, "Improving the spectral resolution of wedged etalons and linear variable filters with incidence angle," *Opt. Lett.* **30**(19), 2647–2649 (2005).
47. C. R. Pidgeon and S. D. Smith, "Resolving Power of Multilayer Filters in Nonparallel Light," *J. Opt. Soc. Am.* **54**(12), 1459–1464 (1964).
48. M. L. Baker and V. L. Yen, "Effects of the Variation of Angle of Incidence and Temperature on Infrared Filter Characteristics," *Appl. Opt.* **6**(8), 1343–1351 (1967).
49. J. Altmann, R. Baumgart, and C. Weitkamp, "Two-mirror multipass absorption cell," *Appl. Opt.* **20**(6), 995–999 (1981).

50. M. Malak, F. Marty, N. Pavy, Y. A. Peter, L. Ai-Qun, and T. Bourouina, "Cylindrical Surfaces Enable Wavelength-Selective Extinction and Sub-0.2 nm Linewidth in 250  $\mu\text{m}$ -Gap Silicon Fabry-Perot Cavities," *J. Microelectromech. Syst.* **21**(1), 171–180 (2012).
51. H. A. Macleod, *Thin-film Optical Filters* (CRC Press, 2010).
52. R. Santbergen, A. H. M. Smets, and M. Zeman, "Optical model for multilayer structures with coherent, partly coherent and incoherent layers," *Opt. Express* **21**(S2), A262–A267 (2013).
53. Z. Knittl, *Optics of Thin Films: An Optical Multilayer Theory* (Wiley, 1976).
54. M. Fritze, J. Knecht, C. Bozler, C. Keast, J. Fijol, S. Jacobson, P. Keating, J. LeBlanc, E. Fike, B. Kessler, M. Frish, and C. Manolatos, "Fabrication of three-dimensional mode converters for silicon-based integrated optics," *J. Vac. Sci. Technol. B* **21**(6), 2897–2902 (2003).
55. A. Piegari, J. Bulir, and A. Krasilnikova Sytchkova, "Variable narrow-band transmission filters for spectrometry from space. 2. Fabrication process," *Appl. Opt.* **47**(13), C151–C156 (2008).
56. A. Emadi, H. Wu, S. Grabarnik, G. De Graaf, and R. Wolffenbuttel, "Vertically tapered layers for optical applications fabricated using resist reflow," *J. Micromech. Microeng.* **19**(7), 074014 (2009).
57. D. D. Arslanov, M. P. P. Castro, N. A. Creemers, A. H. Neerinx, M. Spunei, J. Mandon, S. M. Cristescu, P. Merkus, and F. J. M. Harren, "Optical parametric oscillator-based photoacoustic detection of hydrogen cyanide for biomedical applications," *J. Biomed. Opt.* **18**(10), 107002 (2013).

## 1. Introduction

Optical microelectromechanical systems (MEMS) technology has enabled the design and fabrication of various types of microspectrometers operating at different parts of the spectrum [1,2]. Initial work focused on channel switching for glass fiber communication applications. These devices typically involved an electrostatically tunable Fabry-Perot (FP) resonator that was fabricated using bulk micromachining and silicon wafer bonding [3]. Subsequent studies have proposed grating-based microspectrometers for the visible and near-IR spectral range [4,5], MEMS-based Fourier transform infrared spectroscopy (FTIR) systems [6] and FP-based microspectrometers [7]. A special category can be reserved for the microspectrometer that is based on optical components in a waveguiding layer [8].

An important application of a microspectrometer is in optical absorption spectroscopy, which is a commonly used method for material identification due to its nondestructive and self-referencing properties. For gas sensing it offers a promising compromise between high-resolution and high-cost methods such as gas chromatography, and nonselective and low-cost methods involving calorimetric sensing [9]. In optical absorption spectroscopy light is passed through a sample and the ratio of absorbed to incident radiation is recorded. The sample is identified by comparing the acquired spectrum with a database. The actual spectral position of the series of absorption peaks is unique for each chemical substance, while the amount of optical absorption at each of these peaks is correlated to the concentration of the chemical species. Therefore, the composition of a gas mixture, where each individual gas is characterized by a specific absorption spectrum, can be measured using a spectrometer and multivariate analysis techniques [10]. This method is particularly suitable for the measurement of combustible gases that contain so-called hydrocarbons (methane  $\text{-CH}_4$ , ethane  $\text{-C}_2\text{H}_6$ , etc.) in the mid-IR, because of their unique absorption spectra in this wavelength range.

The microspectrometer system presented here is designed for measuring the composition of natural gas, which has been a major source of energy in the last century for both households and industry. However, the depletion of domestic resources forces many countries to import natural gas. Moreover, sustainable resources such as biogas are gradually being introduced in the gas grid. These trends result in an increased variation in combustible gas composition and requires regular composition measurements for safe combustion and proper billing [11]. This calls for a robust, reliable, and low-cost gas sensor. Because of the wafer-level batch fabrication, a MEMS solution would make this possible, forcing the device to be miniaturized to the chip-level. Although device miniaturization is a recognized advantage and driver of mainstream IC technology, it is not necessarily an advantage in optical devices. For a gas-specific absorption coefficient, the miniaturization makes it challenging to ensure an absorption path of sufficient length. Moreover, one of the main objectives is to realize a system that would be suitable for implementation in any household or industry. This implies a

high-volume application, which puts emphasis on the CMOS-compatibility of the solution [12].

The main components of natural gas are hydrocarbons. The vibrational modes of hydrocarbon molecules are in the mid-IR range, particularly in the 3.1 to 3.7  $\mu\text{m}$  wavelength range as shown in Fig. 1 [13].

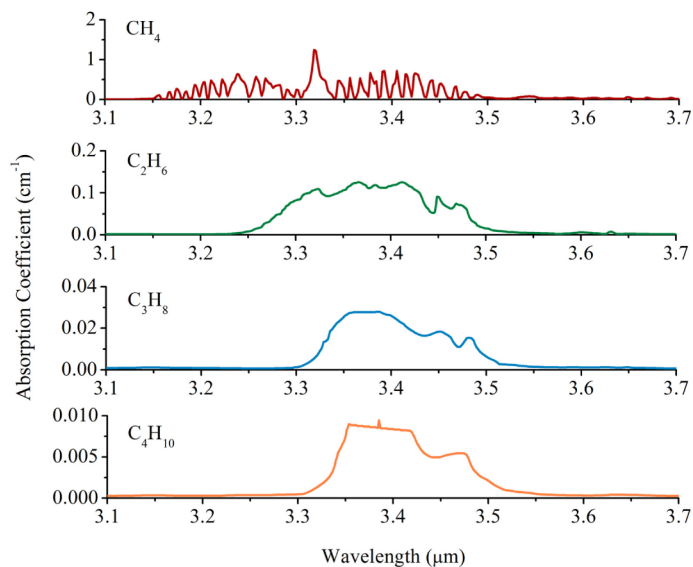


Fig. 1. Absorption coefficients of hydrocarbons calculated using typical natural gas concentrations and the NIST database at room temperature for 1 bar total pressure.

There are in principle two options for realizing a gas analyzer which utilizes absorption spectroscopy. The most significant system aspect is whether the spectral selectivity is implemented in the light source or in the detector. Scanning the spectrum with a tunable light source -either in narrowband with tunable diode-lasers [14] or in wideband using quantum cascade lasers [15]- and selecting one specific wavelength, as is the case in the nondispersive IR (NDIR) gas sensor [16], are two main methods used for implementing spectral selectivity in the light source. The second option is implemented in the detector, where the spectrum is scanned using a wideband source and a tunable narrowband filter at the detector [17]. However, the conventional approach for an IR absorption based spectrometer consists of four essential components: a wideband light source, an optical filter or an interferometer, a sample cell, and a single detector or a detector array, as shown in Fig. 2(a). Several research groups have reported miniaturized light sources [18–20], optical filters [17,21–28], and detectors [29,30]. However, the sample cell which is used for storing the sample gas occupies a large part of the microspectrometer. In this work we achieved a significant miniaturization of the gas IR absorption spectrometer by functional integration of the sample cell with an optical filter as shown in Fig. 2(b) while ensuring a sufficient absorption for practical measurements. Our FP-based microspectrometer uses a long resonator cavity also as the sample cell with highly reflective mirrors that are suitable for multiple reflections.

The FP resonator is a wavelength-selective device that is composed of two parallel flat mirrors with a resonator layer in-between. The optical thickness of the resonator layer determines the wavelength to be transmitted. Wideband operation of the filter must be ensured for high accuracy spectroscopic applications. There are two different implementations of the FP-based microspectrometer. The first is based on a spring-suspended mirror, which is positioned on top of a lower mirror on the substrate and covers a detector. The device is usually fabricated by micromachining and can be vertically deflected, for instance by electrostatic forces [7]. Hence, the size of the airgap in between the mirrors, which is the

thickness of the optical resonating layer, can be controlled. Challenges are in obtaining a mirror that is perfectly parallel with the wafer surface and controlling a large tuning range with limited voltage range. Moreover, a device with movable parts is inherently more vulnerable as compared to an all solid-state device. The alternative is an array of dielectric layers in between Bragg mirrors, each tuned to a particular resonance by a different layer thickness [22]. These fixed-length resonators are more stable and are more compatible with CMOS microfabrication technology. However, the number of resonators in the array defines the spectral resolving power. Fabrication of many resonators, each with a different thickness, in one process flow is a technological challenge.

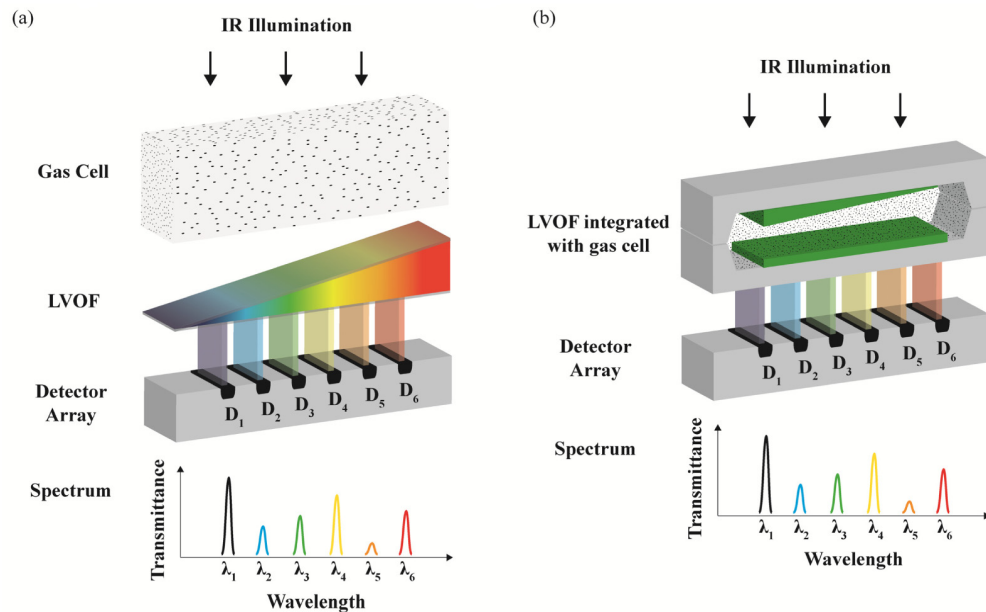


Fig. 2. The components of an optical absorption based spectrometer with (a) a standard LVOF combined with a separate gas cell which requires an optical path length of at least 5 mm, and (b) a miniaturized gas cell integrated with the resonator cavity of an LVOF.

The linear variable optical filter (LVOF) combines the advantage of continuous wavelength scanning of the electrostatically deflected FP resonator with the robustness and CMOS-compatibility of the array of resonators. The LVOF is usually considered an FP optical filter that is composed of one flat and one slightly tilted mirror with a tapered resonator in-between. The resonator thickness varies linearly as the filter is scanned along its length; hence, a wideband spectral response from the filter can be obtained using a detector array. Therefore, using the resonance cavity of an LVOF also as a gas cell is a promising new concept for high reliability, wideband operation and a significant reduction in the size of MEMS-based absorption spectrometers.

In the next section, the requirements of using an LVOF cavity as a gas cell will be discussed. Section 3 investigates the design approach and demonstrates that the Fizeau model is more appropriate than the FP model. The optical design of the device based on the Fizeau approach is presented in section 4, which is followed by a brief summary of the fabrication method. In section 6, the performance of the filter as an NDIR system is demonstrated with actual gas measurements.

## 2. LVOF cavity as a gas cell

Linear variable optical filters have previously been presented as microspectrometers in the visible [23] and mid-IR [24] with tapered silicon dioxide resonator layers. The optical

requirements in LVOF design for the gas filled resonator are different from the typical LVOF design in the sense that a much longer cavity is used, resulting in a higher mode of resonance ( $m > 10$ ). In addition, the multiple reflections imply that the reflectance of the Bragg reflector is higher ( $R > 0.95$ ).

The Beer-Lambert Law states that the attenuation of light (i.e. absorbance) passing through a medium is a linear function of the path length and the concentration of the attenuating species in the medium [31]. An optical path length (*OPL*) of 5 to 10 mm is required for a reasonable absorbance of 30 to 50% that can be detected in the wavelength range of 3.1 to 3.7  $\mu\text{m}$ , where the absorption coefficient of methane oscillates between 0 and 1.2  $\text{cm}^{-1}$  assuming typical natural gas concentration. Hence, the functional integration of the resonator cavity with the sample cell requires a significant path elongation.

The length of the resonance cavity that can be realized using the state-of-the-art MEMS technology depends on the actual technology used and would be the wafer thickness (525–800  $\mu\text{m}$ ) in case of through-wafer etching combined with wafer bonding. The length would be limited to about 50  $\mu\text{m}$  when using bulk micromachining and about 5  $\mu\text{m}$  in surface micromachining, when also considering the fact that the etch stop should be optically smooth. Bulk micromachining is the optimum compromise between the required minimum length that is necessary for enabling the use of the resonator as a gas cell and the fabrication constraints that are imposed by the CMOS-compatibility. It should be noted that the consequences of such dimensional choices to the optical design are significant. Achieving the absorption path length of 5 mm within a resonator cavity of, for instance 25  $\mu\text{m}$ , would require an elongation by a factor of 200 through multiple reflections.

The basic concept of using an absorbing medium in an FP cavity for spectral analysis was first introduced by Jackson [32] for spherical FP interferometers and was later discussed by Kastler [33] for parallel-reflector FP structures. Hernandez [34] studied the effect of an absorbing medium in FP interferometers and concluded that extreme high-finesse reflective coatings would be required to achieve a long path cell behavior. The potential for miniaturization was not considered at the time and practical implementation was not pursued. With the advances in microfabrication technology, it is now possible to fabricate highly reflective mirrors with negligible surface roughness and waviness. It should also be noted that gas-filled FP etalons are commonly used in gas lasers, where a positive optical feedback is required in addition to optical amplification provided by a gain medium [35]. Selective optical feedback is achieved by placing a gain medium between highly reflective mirrors and making use of multiple reflections in the resonator. In the gas absorption spectrometer presented here the gain medium of the gas laser is simply replaced with the absorbing medium to be measured, which would justify the nickname ‘lossy FP etalon’.

The analysis of LVOF-based filters reported in literature is based on the assumption that the LVOF device is basically an FP resonator; albeit one with one of the mirrors tilted (i.e. the mirrors are nonparallel). However, the optical effect of the very small tilt angle is subsequently disregarded. Such a simplification may be acceptable for LVOFs that are designed for operation over a relatively narrow free spectral range (FSR) or for moderate spectral resolution. In such systems, FSR is specified in a moderate value of the coefficient of finesse that directly determines the minimum reflectance requirement for the mirror, typically up to  $R \sim 0.85$ . Similarly a moderate spectral resolution results in a moderate value of the finesse and operation at a low mode of resonance, typically up to  $m \sim 3$ . For LVOF devices that include Bragg mirrors with a high reflectance that operate at a high mode of resonance, this assumption is not valid anymore. Actually, the starting point of a parallel-mirror is also not acceptable in a high-performance electrostatically tunable FP-based microspectrometer, because the tilt angle due to fabrication tolerances would render the conclusions that would be drawn from such an analysis invalid. This mechanism was recognized and has resulted in the use of the term ‘effective finesse’ in literature, which has a reduced value as compared to the theoretical intrinsic finesse by the effect of the mirror nonparallelism [17,36].

However, mirror nonparallelism is inherent to the fundamental operating mechanism of the LVOF-based microspectrometer with a functionally integrated gas cell (absorption

volume) and resonator that is presented here, because of the need for high-reflectance Bragg mirrors combined with the operation at a high mode of resonance, which makes the conventional modeling in terms of an FP resonator inaccurate. As is presented in the next section, the description in terms of the Fizeau interferometer is more appropriate.

### 3. From Fabry-Perot to Fizeau interferometer

Linear variable optical filters have so far been considered an array of discrete fixed cavity length FP filters in analysis using thin-film design tools. However, due to the nonparallelism of the mirrors, the spectral response of an LVOF diverges from the conventional FP filter. The difference becomes especially significant when reflectivity of the mirrors approaches unity. Therefore, it is crucial to study the difference between these two configurations and develop a mathematical framework to assist in the design of an LVOF.

#### 3.1 Theoretical background

##### 3.1.1 Fabry-Perot interferometer

The theoretical background of an FP interferometer is explained by Born and Wolf [37] in detail. Assume that a collimated monochromatic light is impinging on an etalon with refractive index  $n'$  and thickness  $h$  at an incidence angle of  $\theta$  as shown in Fig. 3. The light hits the second flat of the etalon at an incidence angle of  $\theta'$  and the refractive index of the surrounding medium is  $n$ . Then the optical path difference between the first and the  $p$ th wave that is transmitted through the filter is

$$\Delta S_p = (n'(AB + BC) - nAN)(p-1). \quad (1)$$

Using trigonometry and Snell's Law, the optical path difference and subsequently the phase difference ( $\delta_p$ ) between the first and the  $p$ th wave that is transmitted through the filter can be calculated by Eq. (2) where  $\lambda_0$  is the wavelength of the light source. The phase change for reflection at the mirrors is neglected. This could be an issue in metal-based mirrors; however, can be disregarded in dielectric mirrors [38].

$$\delta_p = \frac{2\pi}{\lambda_0} \Delta S_p = \frac{4\pi}{\lambda_0} n' h \cos \theta' (p-1) \quad (2)$$

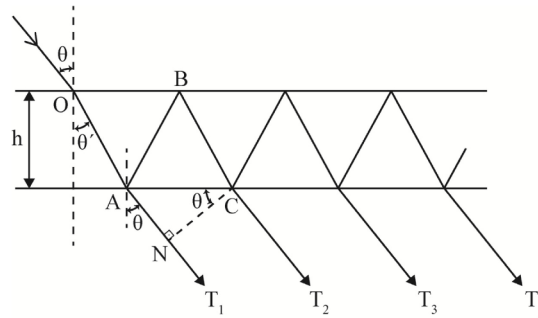


Fig. 3. Fabry-Perot interferometer.

##### 3.1.2 Fizeau interferometer

The Fizeau interferometer can be described as a wedged FP interferometer where one of the mirrors is slightly tilted to create fringes of equal thickness when illuminated with monochromatic light. These interferometers are used for measuring optical flatness with high accuracy [39]. An LVOF can, therefore, be defined as a Fizeau interferometer illuminated with a broadband light source for spectroscopic purposes.

The multiple beam interference of Fizeau wedges was theoretically studied by Brossel [40]. The wedge material is assumed to have a refractive index  $n'$  surrounded with a medium of refractive index  $n$  and with mirror surfaces, of which one is inclined at an angle  $\alpha$ . The device is illuminated with a plane wave of monochromatic light whose wave-fronts are passing through the wedge apex. The angle of incidence  $\theta'$ , is defined as positive when the light impinges on the flat surface from the side of the normal nearest to the wedge apex and negative ( $\phi'$ ) otherwise.

The incident light beam moves away from the wedge apex during multiple reflections in the wedge if the incidence angle is positive [Fig. 4(a)] whereas the beam moves towards the wedge apex if the incidence angle is negative [Fig. 4(b)]. At the  $p$ th reflection from the flat surface, the angle between the beam and the normal would be  $\theta' + 2(p-1)\alpha$  for a positive and  $\phi' - 2(p-1)\alpha$  for a negative incidence angle respectively. Then the exit angle from the wedge for all transmitted waves ( $\theta_1, \theta_2, \dots, \theta_p$ ) can be defined using Snell's Law. Multiple reflections inside the wedge gives rise to a set of plane waves with wave-fronts  $W_1, W_2, \dots, W_p$ , which will interfere at point  $P(x, z)$  as shown in Fig. 4(c) and 4(d) for positive and negative incidences respectively.

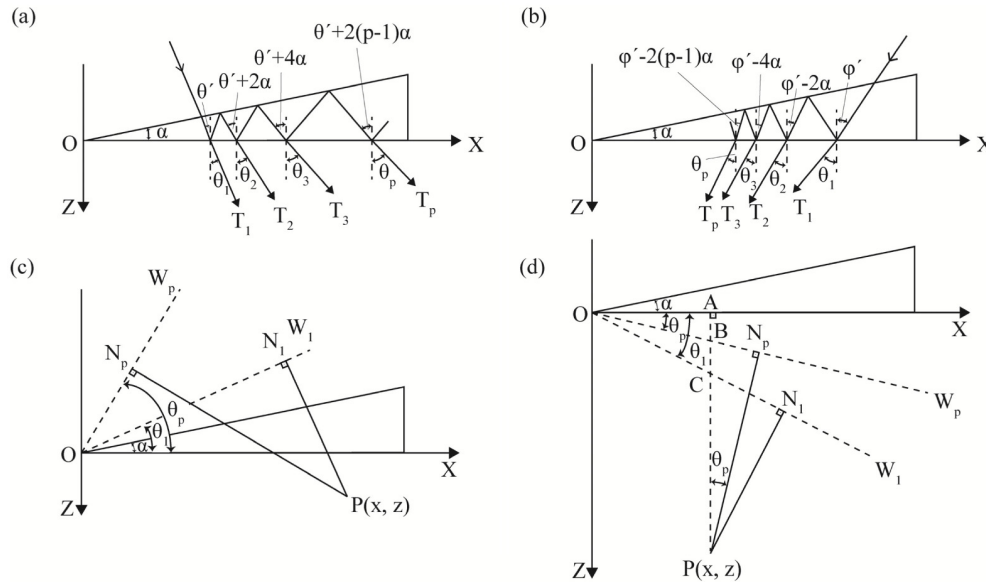


Fig. 4. Multiple reflections in a Fizeau interferometer at (a) positive and (b) negative incidence angle. Optical path difference after multiple reflections in a Fizeau interferometer at (c) positive and (d) negative incidence angle.

The optical path difference between the first and the  $p$ th transmitted wave can be calculated as follows:

$$\Delta S_p = n(PN_p - PN_1) \quad (3)$$

Inserting the exit angles and trigonometric equalities in Eq. (3), one can define the optical path difference in terms of  $\theta'$ ,  $\alpha$ , and  $p$  for both positive and negative incidence ( $\phi' = -\theta'$ ). If the resonator layer and the surrounding medium are both air ( $n = n' = 1$ ) as in our case, the phase difference can be simplified as in Eq. (4).

$$\delta_p = \frac{2\pi}{\lambda_0} \Delta S_p = \frac{2\pi}{\lambda_0} (x [\sin(\theta' + 2(p-1)\alpha) - \sin\theta'] + z [\cos(\theta' + 2(p-1)\alpha) - \cos\theta']) \quad (4)$$

The intensity of infinitely many transmitted waves interfering at point P ( $A^{(i)}$ ) with an incoming wave amplitude of  $A^{(i)}$ , can be calculated using Eq. (5), where  $R$  and  $T$  are the reflectivity and the transmissivity of the mirrors respectively.

$$I^{(i)} = (A^{(i)})^2 T^2 \left| \sum_{p=1}^{\infty} R^{(p-1)} e^{i\delta_p} \right|^2 \quad (5)$$

The spectral response of an FP interferometer can be simulated by sweeping the wavelength for a given cavity length using Eq. (2) and Eq. (5). To calculate the transmittance of a Fizeau interferometer, the  $x$ -position (i.e. the cavity length) must be swept for a particular wavelength using Eq. (4) and Eq. (5).

### 3.2 The effect of operating mode and reflectivity

The transmission of both interferometers is calculated using the theoretical descriptions given in the previous section. Figure 5 shows the simulation results at the 3rd and the 15th order for various reflectivity values. Normal incidence is assumed and interference is observed directly after the interferometer ( $z = 0$ ). For the FP interferometer, a cavity length of respectively 5.085  $\mu\text{m}$  and 25.425  $\mu\text{m}$  is selected. These correspond to the 3rd and the 15th operating orders for a wavelength of 3.39  $\mu\text{m}$ . The 11.4 mm long mirrors of the Fizeau interferometer are inclined at an angle of 15.6 millidegree. The  $x$ -position of the Fizeau interferometer is swept in such a way that the 3rd and the 15th operating orders are captured.

The difference in transmission between the FP and the Fizeau representations are evident from the results. The transmittance of an FP interferometer can theoretically reach 100% at any operating order and reflectivity [Fig. 5(a) and 5(c)], which is not the case for the Fizeau interferometer [Fig. 5(b) and 5(d)]. The resolution of the transmission curves of both the FP and Fizeau interferometers improves with increasing order and reflectivity. At 90% reflectivity, the Fizeau interferometer exhibits a similar performance to the FP interferometer. However, at higher reflectivity values the peak transmittance of the Fizeau interferometer deviates substantially. The reduced transmittance, as compared to the FP, is due to walk-off [41]. Moreover, the transmission curve loses its symmetry and side peaks appear, which are due to the uneven shape of the structure. It should be noted that the reduction of peak transmittance with increased mirror reflectivity is more significant at higher orders of resonance,  $m$ .

A multi-pass gas-filled resonance cavity operating at high order of resonance with highly reflective mirrors is required to enable the use of the LVOF cavity as a gas cell. Both the high-order mode and the high reflectance make it necessary to simulate the transmission at a set of positions on the tapered slope in an LVOF by treating these as positions in a Fizeau interferometer, rather than an array of discrete FP filters.

In addition to the simplified cosine effect of the incidence angle, the effect of filter-detector separation is neglected in the FP approach, while these are important parameters in LVOFs. Moreover, the spectral performance of both the FP and Fizeau interferometers is highly dependent on the collimation of the incident light. In the next subsections it is demonstrated that the LVOF should be simulated using the Fizeau model, while taking into account the effect of mirror reflectivity, operating mode and incidence angle, for an accurate assessment of the effect of filter-detector separation and degree of collimation of the incident light (i.e. the cone angle).

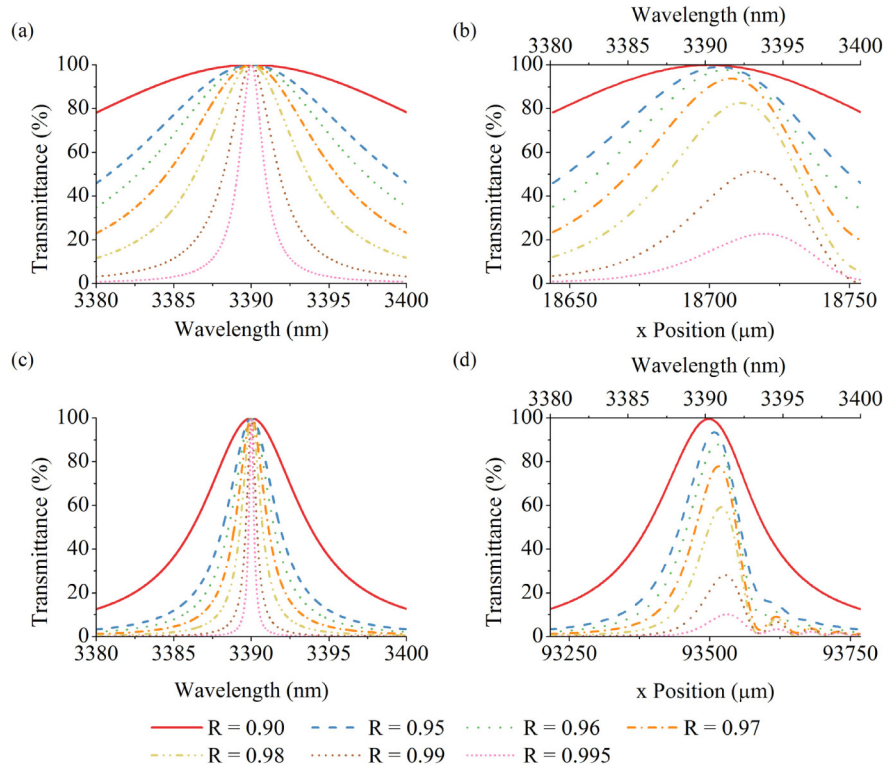


Fig. 5. Comparison of FP and Fizeau interferometers for various reflectivity values at 3390 nm: (a) 3rd order FP interferometer, (b) 3rd order Fizeau interferometer, (c) 15th order FP interferometer, and (d) 15th order Fizeau interferometer.

### 3.3 The effect of incidence angle and filter-detector separation

The sharpness of the fringes in a Fizeau interferometer is highly dependent on the incidence angle of the light. The phase difference between the transmitted waves varies both along the length of the interferometer ( $x$ ) and towards the detector ( $z$ ) depending on the incidence angle. This complex relation was previously studied and it was shown that there is an optimum incidence angle for every interferometer-detector separation where the peak transmittance is maximized [42–45].

Multiple reflections between nonparallel mirrors cause the light to laterally shift and eventually walk out of the wedge shaped cavity. The nonsymmetrical shape of the transmission curves of a Fizeau interferometer that exhibit lower peak transmittance compared to an equivalent FP filter can be explained by this walk-off. The same observation can also be made in numerical simulations: the change in the transmission curve becomes negligible after a certain number of reflections. Therefore the rest of the reflections can be disregarded. As discussed before, a positive incidence angle, at which the angle of reflection increases at each reflection on the tapered mirror, pushes the multiple-reflected light beam away from the wedge apex. In contrast, in the case of a negative angle of incidence, the angle of reflection decreases at each reflection at the tapered mirror and the multiple-reflected light beam is pushed towards the wedge apex. Hence, applying a positive incidence angle on a Fizeau interferometer is similar to enhancing the effect of walk-off, therefore deteriorating the performance. Hence, the optimum incidence angle must be negative to counteract the walk-off effect. However, this doesn't imply that a more negative angle results in a higher peak transmittance. After a number of reflections, the angle of reflection gets so close to zero (i.e. normal incidence) that the reflected beams start to move away from the wedge apex. When

these beams that are reflecting away from the wedge apex cancel the effect of the beams reflecting towards the wedge apex, the transmission curve starts to diverge from the optimum shape again.

The angle of incidence ( $\theta'$ ) was defined as the angle of the light impinging on the flat mirror of the wedge. The trajectory of the beam is illustrated in Fig. 6 for various incidence angles assuming 4 reflections from the flat mirror in each case. For both normal and positive incidence, the reflected beam moves away from the wedge apex with normal incidence giving a sharper curve at a slightly higher transmittance. When changing the angle of incidence between the optimum and normal, the beam is firstly reflected towards the wedge apex, until the angle of normal incidence is reached (or surpassed) and then moves away from the wedge apex. The distinction becomes clear at this point: if the beam passes the  $x$ -position of the initial beam that enters the wedge, the reflections moving away from the wedge apex cancel the effect of the reflections towards the wedge apex. If the reflected beam does not exceed this point, the system is operated at optimum angle of incidence. As the incidence angle gets even smaller than the optimum value (i.e. more negative), the beam gets reflected towards the wedge apex; however, its trajectory resembles the mirrored version of the trajectory of a beam at a positive incidence angle with a smaller value.

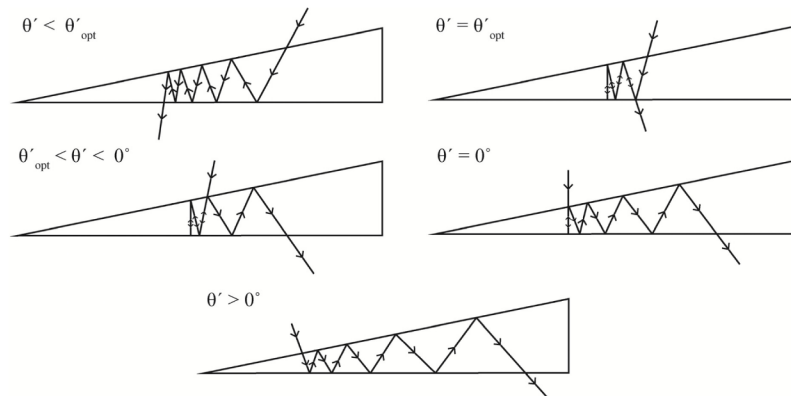


Fig. 6. The trajectory of a beam in a wedge at different values of the angle of incidence. The light beam gets reflected 4 times off the flat mirror in each case.

The spectral response of a Fizeau interferometer with a 15.6 millidegree angle between its mirrors is simulated for various incidence angles as shown in Fig. 7. The  $x$ -position range is selected such that the transmission curve of 3.39  $\mu\text{m}$  wavelength operating at the 15th order is captured. The interference is observed right after the filter, i.e.  $z = 0$  and the reflectivity of both mirrors is 0.985. The optimum incidence angle for this particular case is  $-2.2^\circ$  and it can be observed in Fig. 7 that any incidence angle other than this value results in wider transmission curves with lower peak transmittance. The curves with incidence angles that are higher than the optimum value lean away from the wedge apex while the curves with incidence angles that are lower than the optimum value lean towards the wedge apex. This can be correlated to the trajectory discussion such that any incidence angle smaller than the optimum value directs the beam towards the wedge apex. Moreover, incidence angles higher than the optimum value either first sends the beam towards the wedge apex and then away from the wedge apex or directly away from the wedge apex. The transmission curve for the optimum incidence angle acts as a transition point and looks rather symmetric except for the side peaks. As explained before, a beam with an incidence angle smaller than the optimum value follows a trajectory similar to that of a beam with positive incidence angle with a smaller value. The transmission curves at an incidence angle of  $-5^\circ$  and  $3^\circ$  appear like the mirrored version of each other.

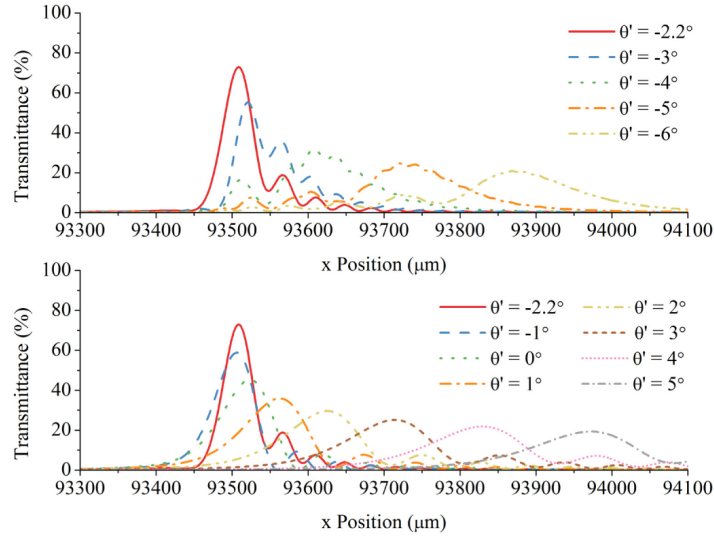


Fig. 7. The transmission curves for a Fizeau interferometer at different values of the angle of incidence.

Rotating a Fizeau interferometer around the wedge apex or changing the incidence angle of the light impinging on the filter is equivalent to rotating the coordinate system of the wedge. Therefore, the effect of filter-detector separation can be analyzed, since the same interference pattern can be observed at different detector planes with different incidence angles. The transmission curves of the Fizeau wedge described above are simulated at normal and optimum incidence for various filter-detector separation values as shown in Fig. 8.

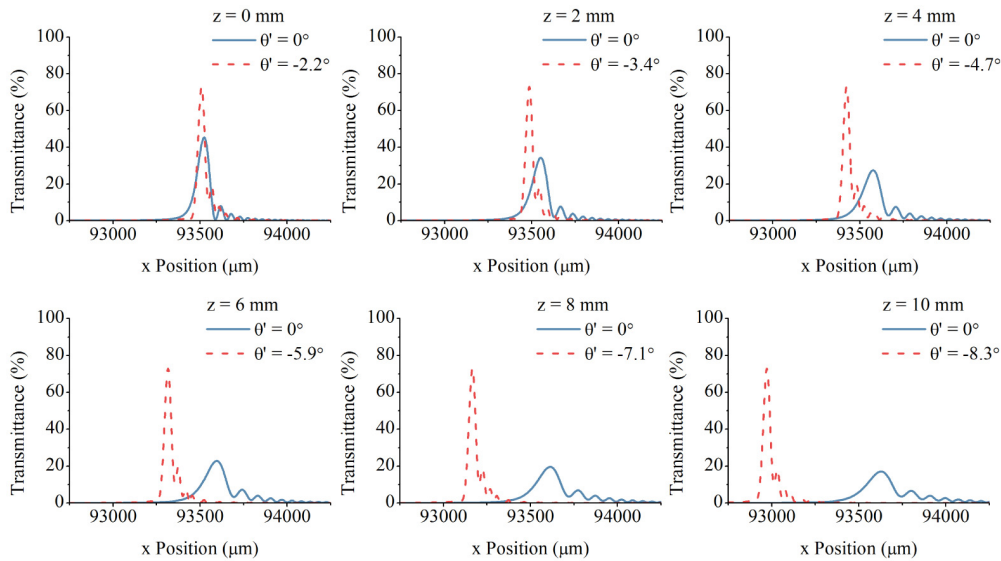


Fig. 8. The effect of filter-detector separation on the spectral response of a Fizeau interferometer.

The incidence angle that would be required for the same optimum transmission curve is at a more negative value with increasing filter-detector separation. The reason is that the  $z$ -position of the beam waist of the interfering waves shifts with the incidence angle and by adjusting the incidence angle, beam width on the detector plane can be minimized to achieve

a narrower transmission curve [46]. A similar reasoning holds for normal incidence; as the detector plane moves away from the filter, the  $z$ -position of the beam waist diverges from the optimum resulting in a wider transmission curve with lower peak transmittance.

Do these results apply to our devices? In an integrated MEMS implementation of an LVOF and a detector array, the filter-detector separation is negligible. However, even if the detector is placed right after the filter, the optimum incidence angle has an offset. Moreover, filter-detector spacing is inevitable in characterization. By studying the discrepancy between theory and experiment at nonzero filter-detector separation, the optimum incidence angle can be adjusted for the final device, where the filter would be right on top of the detector array.

### 3.4 The effect of cone angle

The light source was assumed to be perfectly collimated in the transmission simulations so far. However, a light source can never be fully collimated due to its finite size. Therefore the effect of collimation of the light source should be taken into account in the optical simulations. The effect of collimation of the light on FP filters had been both theoretically and experimentally discussed [47,48]. Due to the cosine effect given in Eq. (2), all the beams except for the one normal to the filter shift the transmission curve to the shorter wavelengths. Hence the overall transmission response of the filter will decrease in amplitude, while shifting to a shorter wavelength than before. For low resolution filters the effect of cone angle is negligible. However, high resolution filters as in this application are very sensitive to even small changes in the cone angle.

A cone of beam with a half cone angle of  $\psi$  and amplitude  $A$  can be described as a collection of  $N$  beams with an amplitude of  $A/N$  and incidence angles ranging between  $-\psi$  and  $\psi$ . By calculating the interference of all these waves, the effect of cone angle on an FP or a Fizeau interferometer can be simulated. In addition to the transmission response of the FP interferometer operating at the 15th order, the Fizeau interferometer that has been introduced before is simulated at  $z = 0$  mm for various half cone angle values divided into a number of beams that correspond to  $0.1^\circ$  steps in the angle of incidence. As shown in Fig. 9, the transmission curves corresponding to  $0.5^\circ$ ,  $1^\circ$  and  $2^\circ$  half cone angle move to shorter wavelengths (or equivalently to smaller  $x$ -position values), while having lower peak transmittance compared to perfect collimation. However, at even higher values of the half cone angle, the peak of the transmission curves start moving slightly to the right since the component normal to the filter dominates the effect of oblique incidence in transmission. The decrease in the peak transmittance on the other hand is linearly linked to the increase in half cone angle where the Fizeau interferometer is less sensitive due to its uneven structure.

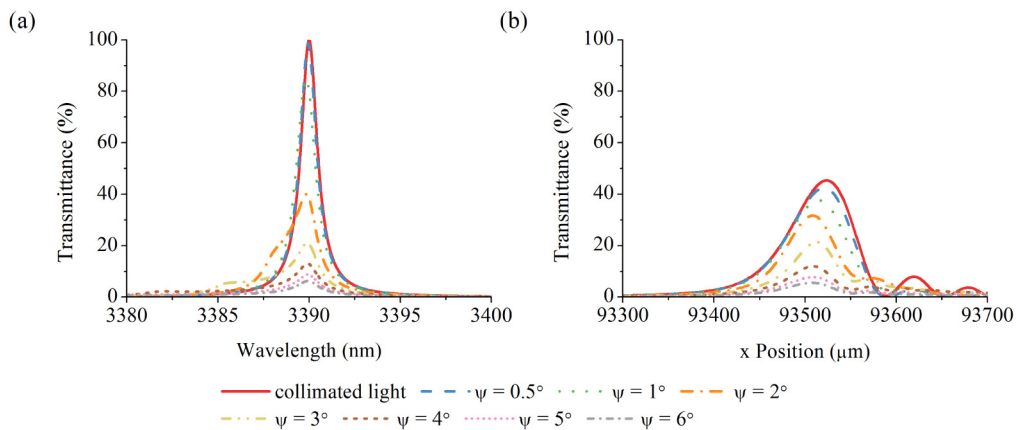


Fig. 9. The effect of cone angle on the spectral response of (a) FP and (b) Fizeau interferometer both operating at the 15th order with a reflectivity of  $R = 0.985$ .

Of the three aspects that have been analyzed using the description of the LVOF in terms of the Fizeau spectrometer, the dependence of the transmittance on the cone angle of the light source is the most performance limiting. This aspect complicates a full spectral analysis of the methane absorption spectrum. For this reason the implementation as a miniaturized NDIR sensor for methane detection is pursued for validating the concept of integrating the gas cell with the LVOF in a MEMS implementation. The nondispersive infrared (NDIR) gas sensor is an absorption spectrometer, where only an optical intensity measurement is done while the spectral selectivity is ensured by the light source. The source is typically a laser that is tuned to the specific absorption line. For methane detection the 3.39  $\mu\text{m}$  line is used due to the availability of the light source. The NDIR system had previously been integrated with a multi-pass absorption cell, which translates an optical path length of 1 m into 3-150 m effective optical path by making use of multiple reflections from concave mirrors [49]. Although such mirrors are complex to fabricate in MEMS technology, preliminary devices are presented in literature [50]. By selecting the appropriate optical channel, the lossy LVOF can therefore be used as a miniaturized NDIR sensor that is functionally integrated with a multi-pass absorption cell.

For such a demanding application, the coherence of the optical system must be considered. Coherence is a property of an optical system that defines the ability to produce an interference pattern. An optical system is referred to as coherent if the interference effect is at maximum while incoherence describes the complete lack of it. The coherence of an optical system depends on the variations in both the light source and the system itself [51]. The coherence length of a light source is proportional to multiplication of the minimum and maximum wavelengths emitted from the source and inversely proportional to the bandwidth. That is why lasers with narrow bandwidths have very long coherence lengths while a wideband source suffers from short coherence length. The coherence length of a light source can be enhanced by filtering the light; hence, limiting the bandwidth. Every optical channel in an LVOF is effectively a narrow-band filter, thus the coherence length of a wideband source is actually improved, thereby allowing the use of a wideband emitter as the light source.

The coherence of the optical system itself on the other hand depends on the optical layers. A thin-film is regarded as coherent while due to its thickness and variations in its thickness, a substrate must be treated as incoherent. The transfer-matrix method used for calculating the optical properties of the mirrors assumes coherent thin-film layers while ignoring the incoherent nature of the substrate which results in unrealistic high-frequency oscillations in reflectivity and transmissivity of the system. These oscillations are not observed in measurements either due to incoherence of the substrate or the limited sensitivity of the measurement. The spectral response that is observed is the average of the high-frequency fringe pattern. To be able to simulate the optical properties of a multi-layer system that contains both coherent and incoherent layers, an additional factor is introduced in the phase difference at equidistant values for incoherent layers followed by averaging at the reflectivity and transmissivity level [52].

#### 4. Optical design

An LVOF must have an initially long cavity and highly reflective mirrors to be able to elongate the optical path of the transmitted interfering waves. The relationship between the cavity length and the bandwidth of an LVOF can be approximated using Eq. (2) if an FP etalon with parallel mirrors is assumed. When the phase difference between two successive waves becomes equal to  $2\pi$ , the spectral response of the filter starts repeating itself. Therefore for normal incidence ( $\theta' = 0$ ) and air cavity ( $n' = 1$ ), Eq. (2) can be simplified to

$$\frac{4\pi}{\lambda_0} h = 2\pi m, \text{ where } m \text{ is the order of interference or the operating order. The distance}$$

between the  $m^{\text{th}}$  and the  $(m+1)^{\text{th}}$  order thus defines the bandwidth of the filter in terms of wavelength, i.e. free spectral range (FSR).

$$FSR_m = \frac{2h}{m} - \frac{2h}{m+1} = \frac{2h}{m(m+1)} \quad (6)$$

A long cavity forces the filter to operate at a higher mode and limits the FSR. The most important changes in the spectra of hydrocarbons occur in 3.2 to 3.4  $\mu\text{m}$  wavelength range, therefore FSR is selected as 200 nm at minimum. Given the fact that the minimum wavelength (3200 nm) is the limiting factor,

$$FSR_m = \frac{2h}{m(m+1)} = \frac{\lambda_{\min} m}{m(m+1)} = \frac{3200\text{nm}}{(m+1)} \geq 200\text{nm}, \quad (7)$$

the operating order must be less than or equal to 15. Using the interference equation, the corresponding cavity lengths at the 15th order can be calculated as 24  $\mu\text{m}$  and 25.5  $\mu\text{m}$  for the minimum and the maximum wavelengths respectively.

The LVOF with one flat and one tapered Bragg reflector which is composed of alternate layers of high and low refractive index materials with quarter wavelength thickness is shown in Fig. 10. To create a taper in the cavity with  $h_1 = 24 \mu\text{m}$  and  $h_2 = 25.5 \mu\text{m}$ , the first layer of the top mirror is tapered and the subsequent layers are deposited normally. When bonded to another wafer with a flat mirror in a cavity, they form an LVOF with a tapered airgap.

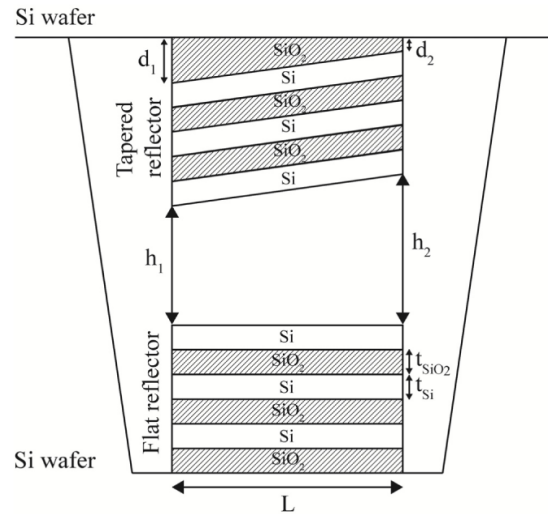


Fig. 10. A schematic illustration showing the cross-section and layer stack of the linear variable optical filter.

Increasing the number of thin-film pairs in a Bragg mirror increases the reflectivity while limiting FSR. A high refractive index contrast between the mirror materials on the other hand improves both reflectivity and FSR. Silicon ( $n_{\text{Si}} = 3.61$ ) and silicon dioxide ( $n_{\text{SiO}_2} = 1.45$ ) are selected as mirror materials due to their adequate refractive index contrast and nonabsorptive ( $k = 0$ ) properties in the intended wavelength range. Considering the fabrication tolerance and uneven structure of the tapered mirror, 3-pair design is selected to achieve high reflectivity as required for the application, while maintaining a power-bandwidth product that enables sufficient signal to the detector at the output of the filter.

To create the required cavity length along the filter, the level difference between the thickest and the thinnest part of the tapered silicon dioxide layer must match the cavity length difference of 1.5  $\mu\text{m}$ . The thickness of the tapered silicon dioxide layer is thus selected to range from  $d_2 = 960 \text{ nm}$  to  $d_1 = 2460 \text{ nm}$  to align the maximum reflectivity to the reference wavelength of 3300 nm. The rest of the silicon dioxide layers of the tapered mirror are  $t_{\text{SiO}_2} = 569.97 \text{ nm}$  thick. The thickness of the silicon layers used in both mirrors is  $t_{\text{Si}} = 228.41 \text{ nm}$ .

The latter two were calculated using the reference wavelength of 3300 nm. The reflectivity and transmissivity values required to calculate the filter transmission are calculated for both FP filter and LVOF assuming 3-pair silicon/silicon dioxide mirrors using the transfer-matrix method while taking into account the polarization and the effect of thick silicon wafer [53].

The reflectivity and transmissivity of the FP filter is almost constant over 3.2 to 3.4  $\mu\text{m}$  wavelength range as shown in Fig. 11. There is a slight decrease in reflectivity and increase in transmissivity away from 3300 nm, since the values for the physical thicknesses of the layers are calculated according to the reference wavelength of 3300 nm. The Fizeau or the LVOF on the other hand has a wavelength dependent reflectivity and transmissivity due to the tapered mirror. As discussed in the theory section, such a small change (1%) in reflectivity might be negligible for many applications; however, it must be taken into account in LVOFs where highly reflective mirrors are required. The effect of polarization is negligible for both configurations, even in the case of a nonzero incidence angle.

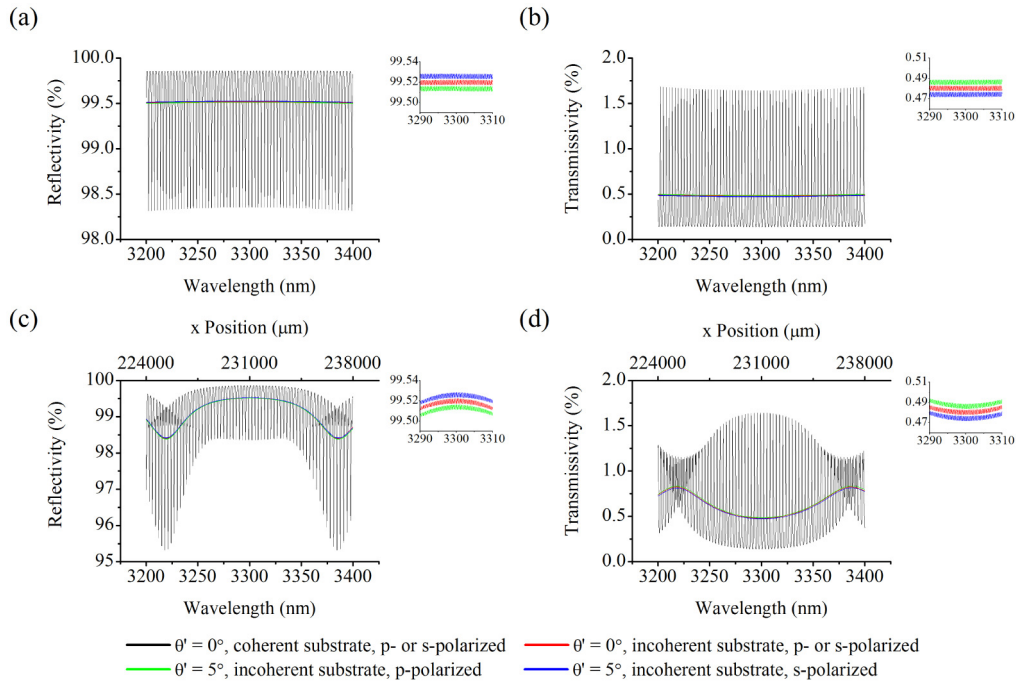


Fig. 11. The reflectivity and transmissivity of FP (a, b) and Fizeau (c, d) filters in the 3.2-3.4  $\mu\text{m}$  wavelength range.

## 5. Device fabrication

The fabrication of an LVOF with air cavity relies on fabricating the flat and the tapered mirrors separately and subsequent wafer bonding [Fig. 12]. The key step of the process is to create a taper with a very small slope. Gray-scale lithography [54] and mechanically moving the mask [55] were conventionally used methods to create tapered thin-film layers. However, gray-scale lithography has high cost especially with increasing resolution and mechanically moving the mask is a time consuming process that requires alteration in the lithography equipment.

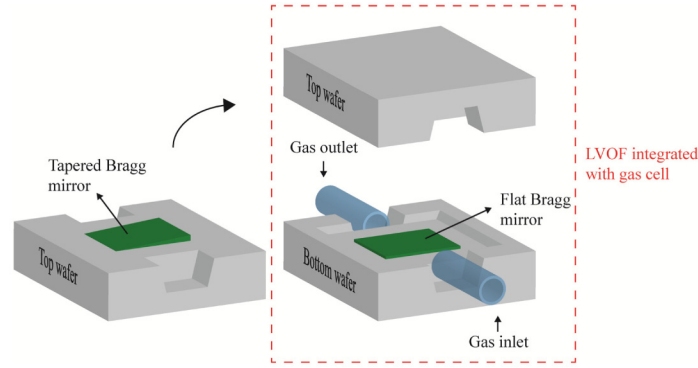


Fig. 12. Schematic illustration of the device assembly.

A CMOS compatible method using conventional fabrication techniques was developed by Emadi *et al.* using linearly variable distanced trenches in photoresist [56]. This method is based on the principle that the volume of a trench must be equal to the volume of the photoresist on both sides of the trench that must be removed to obtain the desired slope [Fig. 13(a)]. The flat photoresist layer with trenches is then converted to a tapered structure by a thermal-chemical treatment. Subsequently, the profile of the photoresist is transferred to the desired optical layer lying underneath by one-to-one plasma etching. This fabrication method has previously been used for tapering resonator layers in LVOFs [23,24]. In this paper, the same method is used to taper the first layer of the tapered Bragg mirror.

To compensate for the process tolerances and to minimize the effect of wafer bending on filter performance, the aimed level difference of  $1.5 \mu\text{m}$  has been doubled. The tapered mirror mask is designed to create a  $3 \mu\text{m}$  level difference on the silicon dioxide layer with  $6 \mu\text{m}$  thick resist. The width of the trenches is selected as  $2 \mu\text{m}$  based on the smallest feature size of the contact aligner and the density of these trenches is varied along the length of the filter. The distribution of the trenches in  $6 \mu\text{m}$  thick positive photoresist (AZ9260) can be seen in the microscope image in Fig. 13(b).

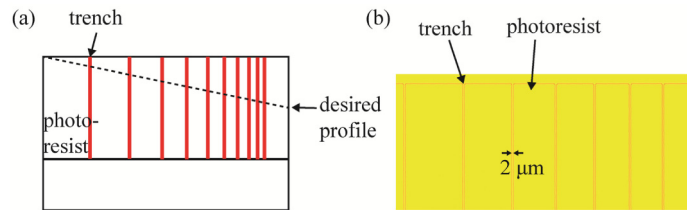


Fig. 13. (a) Fabrication method for creating a tapered optical layer. (b) Microscope image of the photoresist after lithography and development.

## 6. Characterization

A broadband measurement system with the required collimation was not available in the desired wavelength range; therefore, a characterization setup with a highly collimated monochromatic light source is built for measuring the spectral performance of the LVOFs.

### 6.1 System set-up and calibration

An optical setup with a collimated He-Ne laser at  $3.39 \mu\text{m}$  is built to measure the spectral response of the LVOF and to validate the theoretical discussion. An optical chopper that operates at  $1 \text{ kHz}$  is placed after the laser to improve the signal-to-noise ratio. After the optical chopper, a beam steering mirror mounted on a motorized rotational stage is used to steer the beam for the intended angle of incidence. The optical filter to be characterized is

mounted on a motorized linear stage and moved along its length. Lastly, a large area lead selenide (PbSe) detector (ET-6000, Electro-Optics Technology, Inc., USA) with a 15  $\mu\text{m}$  wide and 3 mm long slit is mounted on another motorized linear stage for proper position monitoring during consecutive measurements. The detector signal is band-pass filtered to allow the signal at only 1 kHz to pass by cascading a high- and a low-pass filter (SR650, Stanford Research Systems, USA). The filtered signal is then recorded with a high-performance digital multimeter (Keithley 2002, Keithley Instruments, Inc., USA).

The measurement is done by first aligning the detector with the laser such that the maximum signal is obtained. Then the filter is brought back in the light path and the position range on the filter that corresponds to the transmission curve at 3.39  $\mu\text{m}$  is searched. This range is scanned by moving the filter along its length so that the curve is fully captured. The step size of the movement is selected as 15  $\mu\text{m}$ , same as the slit width, to avoid any convolution effect or missing data.

The measurement results at filter-detector separation  $z = 6$  mm are shown in Fig. 14 for various incidence angles. Due to the repetitive movement of the filter in and out of the light path, each measurement takes about 1 hour. To avoid the effect of possible overheating on filter performance, two scans were taken after turning on the laser that were later averaged to calculate the transmission response. Then the laser was turned off for half an hour to cool down. The  $x$ -position in this setup indicates the position on the filter where the curve that corresponds to 3.39  $\mu\text{m}$  is located. The shift in the  $x$ -position of the filter, which results from the angular positioning of the beam steering mirror, is corrected for different values of the angle of incidence in the measurement results.

The transmission curve at normal incidence exhibits a low peak transmittance with side peaks emerging away from the wedge apex, which is in agreement with the theoretical analysis. As the incidence angle gets smaller, the transmission curve starts moving towards the wedge apex with an increasing peak transmittance. At the optimum incidence angle, the peak transmittance reaches 40% while the top part of the curve becomes significantly narrow. The FWHM of this curve is measured as 105  $\mu\text{m}$  in the  $x$ -position, which corresponds to 4.1 nm spectral resolution. When the incidence angle is further decreased, the peak transmittance starts to get lower and the curve leans away from the wedge apex as expected.

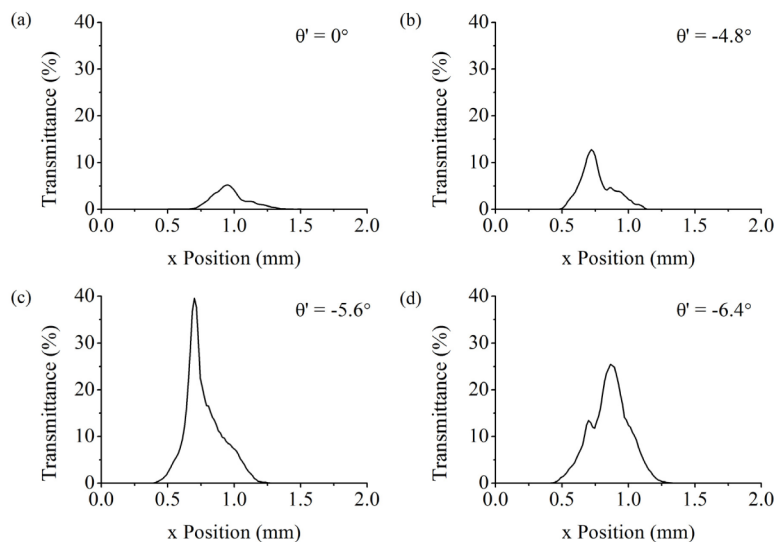


Fig. 14. Measured transmission curves at (a) normal incidence, (b)  $\theta' > \theta'_{\text{opt}}$ , (c)  $\theta' = \theta'_{\text{opt}}$ , and (d)  $\theta' < \theta'_{\text{opt}}$ .

The device was simulated using the real cavity length that was measured with a stylus profiler, at  $z = 6$  mm for various incidence as shown in Fig. 15. The step size in the  $x$ -position

was selected as 1  $\mu\text{m}$  in calculations. The simulated spectral response has been averaged to a single value over every 15 data points to be consistent with the measurement that has been performed with a 15  $\mu\text{m}$  wide slit. The simulated optimum incidence angle is higher than the measured value; however, the curves confirm the shapes and shifts in position. The deviations in peak transmittance are mainly due to fabrication tolerance of the Bragg mirror layer deposition and the nonlinearity in the LVOF taper due to imperfect reflow during fabrication.

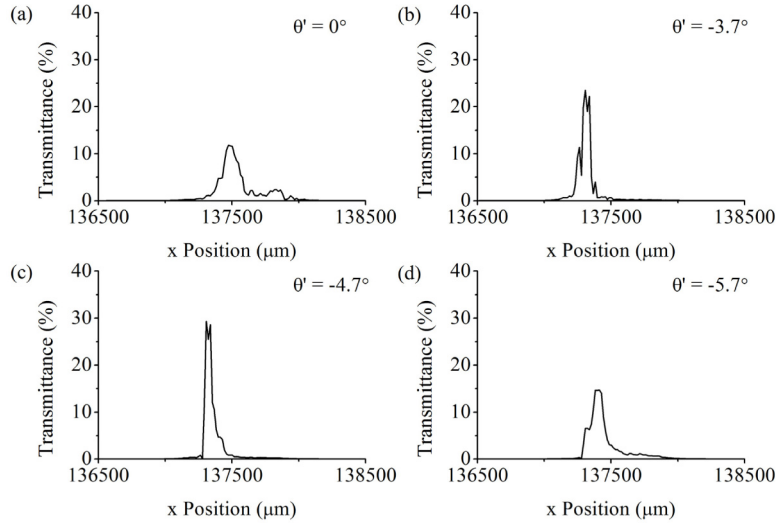


Fig. 15. Simulated transmission curves at (a) normal incidence, (b)  $\theta' > \theta'_{\text{opt}}$ , (c)  $\theta' = \theta'_{\text{opt}}$ , and (d)  $\theta' < \theta'_{\text{opt}}$ .

## 6.2 Gas measurements

The effect of optical path elongation can correctly be characterized if the sample gas is present only in the cavity of the LVOF. To selectively flow gas in the cavity, dispensing tips are glued to the gas inlet and outlet using silicone [Fig. 16(b)]. The inlet is connected to the gas bottle via flexible tubing while the outlet tubing is left open away from the measurement area. The gas flow through the cavity is ensured by applying a pressure of a few mbar above the atmospheric pressure to the gas inlet.

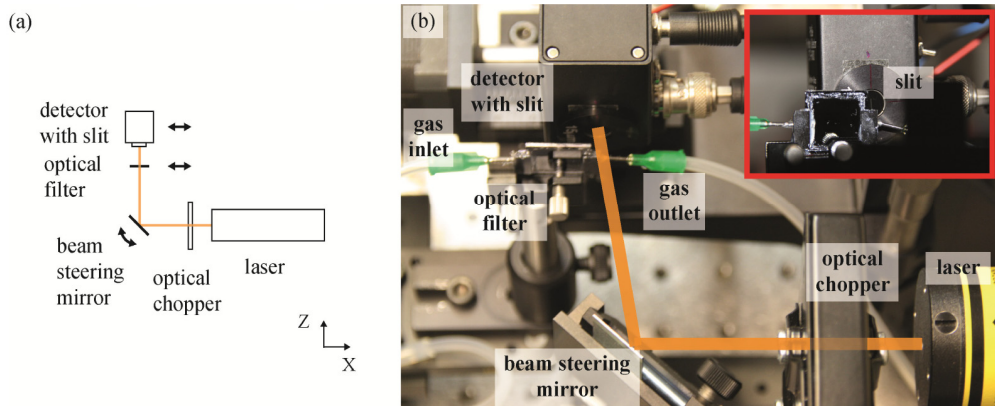


Fig. 16. (a) The drawing of the optical characterization setup. (b) The actual optical characterization setup for gas measurements. The optical filter and slit are shown in detail in the inset.

The same laser measurement procedure has been employed for the gas experiments. Thanks to the flexible tubing the repetitive mechanical movement of the filter holder did not disturb the measurements. To avoid the effect of a possible gas leakage on the optical performance, a fan was placed on top of the filter.

The position of a transmission curve depends strongly on the cavity length and a small perturbation could shift the curve to another position. During the measurements we observed that due to the pressure of the gas in the cavity, the mirrors on each side were pushed outwards. The resulting increase in the cavity length shifted the x-position of the transmission curve. Therefore, a comparison between the transmission of the filter at ambient pressure to the filter with methane above the ambient pressure is not valid, since the optical performance of the latter could be affected by the physical influence of the gas pressure. To overcome this, the filter measurement at ambient pressure was replaced with a measurement using a nonabsorptive gas, nitrogen in this case, at the same experimental conditions as the methane measurement. Thus the physical effect of the gas pressure would be the same for both measurements.

The transmission curves of the filter at  $3.39\ \mu\text{m}$  with methane and nitrogen in the cavity are shown in Fig. 17. Because of the dispensing tips the detector had to be placed further than 6 mm, resulting in a smaller optimum incidence angle of  $-8.8^\circ$ . The peak transmittance of the reference measurement with nitrogen (39.9%) is in agreement with the theory in the sense that the same optimum transmission curve can be found at a different incidence angle for every filter-detector separation.

Compared to the high peak transmittance of nitrogen, methane absorbs almost 80% of the light with a 7.8% peak transmittance. The slight positional shift in the peak transmittance of the two measurements arises from the pressure setting. The output pressure of the gas bottle is adjusted manually using a valve while reading the value on an analog gauge. The pressure displayed on the gauge was 7 mbar and 5 mbar above the ambient pressure for methane and nitrogen respectively, thereby explaining the minor shift in the position of the peak.

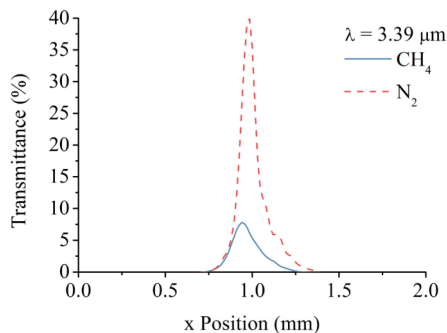


Fig. 17. The measured transmission response of the LVOF at  $3.39\ \mu\text{m}$  with methane and nitrogen in the cavity.

The concentration sensitivity of an optical absorption based gas sensor is mainly driven by the performance of the detector element. In these measurements, a limited part of a commercial large-area detector is used as a single detector element and the spectral response is recorded by scanning the filter along its length. In the final device, the LVOF will be fabricated on top of a detector array and the sensitivity of the whole system will then be defined by the detector performance. The cross-sensitivity of the microspectrometer to a sample in a mixture on the other hand, is highly dependent on the wavelength selectivity of the filter. As indicated in Fig. 1, all hydrocarbons have a significant absorption at  $3.39\ \mu\text{m}$  wavelength. Therefore, it is not possible to selectively detect methane in natural gas only at this spectral position. This wavelength was originally selected due to the availability of the light source for demonstrating the performance of the filter.

The final intended device is a microspectrometer that is capable of measuring the spectrum of a gas mixture in 3.2 to 3.4  $\mu\text{m}$  wavelength range. As shown in Fig. 1, hydrocarbons have distinctive spectral features that can only be captured with a high-resolution filter. Methane absorbs light in the 3.2 to 3.25  $\mu\text{m}$  wavelength window where higher hydrocarbons are nonresponsive. The absorption curves of ethane and propane start at 3.25 and 3.3  $\mu\text{m}$  respectively. Butane and propane have very similar spectral response in addition to having very low concentration in natural gas compared to methane and ethane. Therefore, the combined concentration of butane and propane is usually demanded by the natural gas industry rather than the individual values.

To demonstrate the wavelength selectivity of the LVOF, two more measurements at 3.22  $\mu\text{m}$  and 3.27  $\mu\text{m}$  wavelength have been performed as shown in Fig. 18, using a benchtop optical parametric oscillator (OPO) laser setup [57]. By thermally tuning the refractive index of the nonlinear optical crystal, the wavelength of the laser can be altered. The output of this experimental laser setup is integrated as the light source in our characterization setup. The pure gases flowing into the cavity are at the atmospheric pressure. The filter is scanned along its length and two measurements are averaged for each transmission curve. The absorption of methane is lower compared to the absorption at 3.39  $\mu\text{m}$ , due to the lower, wavelength-specific absorption coefficient of the gas.

The spectral scans at 3.22  $\mu\text{m}$ , 3.27  $\mu\text{m}$  and 3.39  $\mu\text{m}$  confirm that the LVOF integrated with a gas cell could serve as a chip-level microspectrometer that is capable of distinguishing methane from higher hydrocarbons when combined with a broadband light source and a detector array.

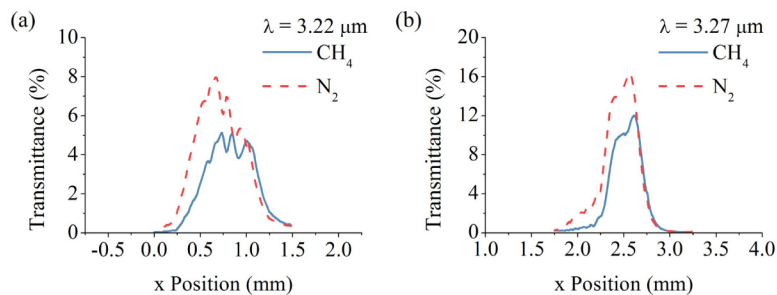


Fig. 18. The measured transmission response of the LVOF at (a) 3.22  $\mu\text{m}$  and (b) 3.27  $\mu\text{m}$  wavelength with methane and nitrogen in the cavity. A mid-IR OPO laser is used as the light source.

## 7. Conclusions

The feasibility of a MEMS implementation of a functionally integrated gas cell and LVOF has been demonstrated. Due to the demanding requirements of the application, the optical design approach has been revisited. It was shown that an LVOF with highly reflective mirrors that operates at a high order must be designed using the Fizeau approach, where the nonparallelism of the mirrors is taken into account, rather than treating it in the conventional approach; as an array of FP filters. Using a mathematical model based on the Fizeau approach; the effect of the mode of operation, reflectivity of the mirrors, angle of incidence, filter-detector separation and cone angle of the light on the spectral response has been investigated. The cone angle of the light source was found as the most limiting factor; thereby, encouraging us to use a well-collimated light source to confirm our simulations. An optical setup with a HeNe laser at 3.39  $\mu\text{m}$  has been built and it has been experimentally shown that the optimum transmission curve (i.e. the narrowest curve with the highest peak transmittance) can be found for every filter-detector separation at different incidence angles. At a filter-detector separation of  $z = 6$  mm, the optimum transmission curve was measured with a peak transmittance of almost 40% and 4.1 nm FWHM resolution. Measurements with

methane were performed using the same setup at 3.39  $\mu\text{m}$ . Compared to the transmission with nitrogen, which is a nonabsorptive gas in the infrared, the filter filled with methane exhibited a significant amount of absorption, therefore confirming the application as an NDIR sensor. Moreover, the wide wavelength performance of the device has been demonstrated using a mid-IR OPO laser as the light source and scanning the filter along its length at 3.22  $\mu\text{m}$  and 3.27  $\mu\text{m}$ .

### **Acknowledgments**

This work has been supported by the Dutch technology foundation STW under grant DEL.11476 and the Energy Delta Gas Research (EDGaR) program. The devices have been fabricated at DIMES Technology Centre of TU Delft and Nanofabrication Laboratory of Chalmers University of Technology. The authors would like to thank Mohammad Amir Ghaderi for his help during fabrication and René H. Poelma for helping with the gas measurements.